Central WENO Schemes for Hamilton-Jacobi Equations on Triangular Meshes

Doron Levy* Suhas Nayak† Chi-Wang Shu‡ Yong-Tao Zhang§

July 19, 2004

Abstract

We develop the first semi-discrete central schemes for Hamilton-Jacobi equations on triangular meshes. High-order schemes are then obtained by combining our new numerical fluxes with high-order WENO reconstructions on triangular meshes. The numerical fluxes are shown to be monotone in certain cases. The accuracy and high-resolution properties of our scheme are demonstrated in a variety of numerical examples.

Key words. Hamilton-Jacobi equations, central schemes, unstructured grids.

AMS(MOS) subject classification. Primary 65M06; secondary 35L99.

1 Introduction

We consider Cauchy problems for Hamilton-Jacobi (HJ) equations of the form

$$\begin{cases} \phi_t(x,t) + H(\nabla\phi(x,t)) = 0, \quad x \in \Omega \subset \mathbb{R}^2, \\ \phi(x,t=0) = \phi_0(x). \end{cases} \tag{1.1}$$

It is well known that solutions of (1.1) may develop discontinuous derivatives in finite time and hence it is necessary to interpret solutions of (1.1) in an appropriate weak sense. Such a formulation in terms of the so-called viscosity solutions is due to Crandall, Evans, Ishii, Lions,... (see [10, 11, 24] and the references therein).

We are interested in approximating solutions of (1.1) on a given conforming triangulation of the domain Ω. While general theory for approximating solutions of (1.1) can be found in the works of Barles, Lions, and Souganidis [4, 31, 25], in this work we focus on Godunov-type schemes for approximating such problems. Godunov-type schemes are based on a global reconstruction which is evolved exactly in time and sampled at the grid nodes at the next time step. A sub-class

*Department of Mathematics, Stanford University, Stanford, CA 94305-2125; dlevy@math.stanford.edu
†Department of Mathematics, Stanford University, Stanford, CA 94305-2125; nayak@math.stanford.edu
‡Division of Applied Mathematics, Brown University, Providence, RI 02912; shu@dam.brown.edu
§Department of Mathematics, UC Irvine, Irvine, CA 92697; zyt@math.uci.edu

of these schemes are central schemes in which the evolution stage is carried out at points that are located away from the discontinuities. Such a procedure eliminates the necessity to deal with (generalized) Riemann problems on the cell-interfaces, which make central schemes particularly suitable for multi-dimensional problems and complicated geometries.

We briefly recall the related central schemes for HJ equations on Cartesian meshes. Second-order fully-discrete central schemes were introduced by Lin and Tadmor [22, 23] (see also [7]). These schemes were extended to high-orders using suitable weighted essentially non-oscillatory (WENO) reconstructions by Bryson and Levy [8]. These reconstructions are based on the WENO schemes by Liu *et al.* [26] and by Jiang and Shu [16] which extend the ENO schemes of Harten *et al.* [13].

Semi-discrete central schemes (on Cartesian meshes) were derived by Kurganov and Tadmor [20]. The main goal there was to reduce the numerical dissipation by estimating the local speeds of propagation of information from the interfaces between neighboring computational cells. The numerical dissipation in these schemes was further reduced by keeping an even more accurate account over the different local speeds [19]. Bryson and Levy increased the order of accuracy of these schemes up to fifth-order by combining the semi-discrete numerical fluxes with WENO reconstructions [9]. This work also provided the theoretical foundation for the monotonicity of the fluxes of [19, 20]. A version of this schemes with even less numerical dissipation was recently derived in [6].

We would like to recall some of the related works on upwind schemes for HJ equations. These include the essentially non-oscillatory (ENO) schemes of Osher, Sethian and Shu [28, 29], and the WENO schemes of Jiang and Peng [15]. Similar methods on triangular meshes include the pioneering works of Abgrall *et al.* [1, 2, 3], Barth and Sethian [5], Kossioris *et al.* [18], and the recent work of Zhang and Shu [32] on WENO schemes for HJ equations on triangular meshes. The high-order WENO reconstructions on triangular meshes that were used in [32] were based on the results of Hu and Shu [14].

In this paper we present the first semi-discrete central scheme for approximating solutions of (1.1) on triangular meshes. Our scheme combines a new numerical flux (that was announced in [21]) with the high-order WENO reconstructions of [32].

The structure of this paper is as follows: We start in Section 2 with the derivation of the numerical flux for HJ equations on triangular meshes. A couple of examples of high-order reconstructions on triangular meshes are then discussed in Section 3. Numerical examples that verify the expected order of accuracy of the schemes as well as the high-resolution properties of the resulting solutions are given in Section 4. Concluding remarks summarize this work in Section 5.

Acknowledgment: We would like to thank Adam Oberman for helpful discussions. The work of D. Levy was supported in part by the National Science Foundation under Career grant No. DMS-0133511. The work of C.-W. Shu was supported in part by ARO grant DAAD19-00-1-0405, NSF grant DMS-0207451, and AFOSR grant F49620-02-1-0113.

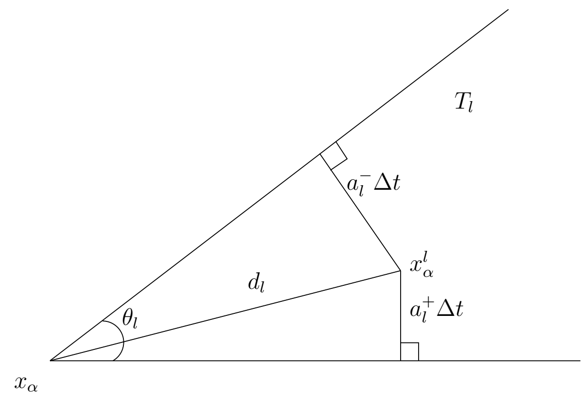

Figure 2.1: Evolution point, x_α^l, derived from the maximal local speeds of propagation into T_l, a_l^+ and a_l^-.

2 Central Schemes for Hamilton-Jacobi Equations

2.1 The Scheme

We consider the two-dimensional HJ equation (1.1), and assume a given triangulation, $\mathcal{T}$, of Ω. We denote the grid points by x_α and assume that every such point is surrounded by m_α angular sectors T_l^α that are ordered counterclockwise. For simplicity we use the simpler notation $T_l = T_l^\alpha$ (see Fig. 2.1).

Given a time-step, Δt, we denote the approximate value at time $t^n = n\Delta t$ of $\phi(x_\alpha, t^n)$ by φ_α^n. Assuming that the values of φ_α^n at the grid-points x_α are known, we reconstruct a continuous piecewise-polynomial interpolant $\tilde{\varphi}_\alpha$. This interpolant has discontinuous gradients along the cell-interfaces. We denote the approximation of the gradient at x_α that is obtained from the reconstruction in the cell T_l by $\nabla\tilde{\varphi}_{\alpha,l}$. For the purpose of developing the numerical flux there is no need to assume any particular reconstruction. Admissible reconstructions will be described in Section 3.

The reconstruction $\tilde{\varphi}_\alpha$ can now be used to estimate the maximal speeds of propagation of information from the cell-interfaces in a direction that is perpendicular to the interfaces. In every sector, T_l, we denote the counterclockwise speed of propagation by a_l^+ and the speed of propagation on the other interface is a_l^- (see Fig. 2.1). These speeds can be estimated by

$$\begin{aligned} a_l^+ &= \max\left\{\max_{T_l}\left\{|\nabla H(\nabla\tilde{\varphi}_{\alpha,l})\cdot\vec{n}_{l-1,l}|\right\}, \max_{T_{l-1}}\left\{|\nabla H(\nabla\tilde{\varphi}_{\alpha,l-1})\cdot\vec{n}_{l-1,l}|\right\}\right\} \\ a_l^- &= \max\left\{\max_{T_l}\left\{|\nabla H(\nabla\tilde{\varphi}_{\alpha,l})\cdot\vec{n}_{l+1,l}|\right\}, \max_{T_{l+1}}\left\{|\nabla H(\nabla\tilde{\varphi}_{\alpha,l+1})\cdot\vec{n}_{l+1,l}|\right\}\right\}. \end{aligned} \tag{2.1}$$

Here, $\vec{n}_{j,l}$ is the normal vector on the interface between T_j and T_l pointing into T_l.

The evolution stage of Godunov-type schemes will be carried out at points x_α^l that are located away from the interfaces, assuming that the time-step is sufficiently small (see Fig. 2.1). The distance of the evolution point x_α^l from x_α is denoted by d_l. Clearly, d_l depends on the local speeds of propagation $a_l^\pm$ and on the angle θ_l. A straightforward computation allows us to define d_l as

$$d_l = \Delta t\hat{d}_l, \tag{2.2}$$

where

$$\hat{d}_l^2 = \frac{(a_l^-)^2 + 2a_l^- a_l^+ \cos\theta_l + (a_l^+)^2}{\sin^2\theta_l}. \tag{2.3}$$

We now evolve the interpolant $\tilde{\varphi}(\vec{x}, t^n)$ to the next time step t^{n+1} at the points x_α^l according to (1.1). Since the evolution points are located away from the propagating discontinuities, the value at the next time-step can be approximated with a first-order Taylor expansion in time, i.e.,

$$\varphi(x_\alpha^l, t^{n+1}) = \tilde{\varphi}(x_\alpha^l, t^n) - \Delta t H(\nabla\tilde{\varphi}(x_\alpha^l, t^n)) + O(\Delta t^2). \tag{2.4}$$

Here, the value of the gradient, $\nabla\tilde{\varphi}(x_\alpha^l, t^n)$, is obtained from the reconstruction, $\tilde{\varphi}$. Expressions of the form (2.4) hold for every evolution point, x_α^l, around x_α.

In order to combine all these values of φ into one value φ_α^{n+1}, we write a convex combination of the values from the different sectors with weights $s_l \geq 0$ that are yet to be determined:

$$\varphi_\alpha^{n+1} = \frac{\sum_{l=1}^{m_\alpha} s_l \varphi(x_\alpha^l, t^{n+1})}{\sum_{l=1}^{m_\alpha} s_l} = \frac{\sum_{l=1}^{m_\alpha} s_l \left[\tilde{\varphi}(x_\alpha^l, t^n) - \Delta t H(\nabla\tilde{\varphi}(x_\alpha^l, t^n)\right]}{\sum_{l=1}^{m_\alpha} s_l}. \tag{2.5}$$

If we now define ρ_l to be the unit vector in the direction of x_α^l from x_α, we can utilize a Taylor expansion in space

$$\tilde{\varphi}(x_\alpha^l, t^n) = \tilde{\varphi}(x_\alpha, t^n) + d_l \rho_l \cdot \nabla\tilde{\varphi}(x_\alpha^l, t^n) + O(\Delta t^2).$$

Here by $\nabla\tilde{\varphi}(x_\alpha^l, t^n)$ we refer to the value of the gradient at x_α that is associated with the reconstruction in sector T_l at x_α^l. We may therefore rewrite (2.5) as the fully discrete scheme

$$\varphi_\alpha^{n+1} = \tilde{\varphi}_\alpha^n + \frac{\Delta t}{\sum_{l=1}^{m_\alpha} s_l} \sum_{l=1}^{m_\alpha} s_l \left[\hat{d}_l \rho_l \cdot \nabla\tilde{\varphi}(x_\alpha^l, t^n) - H(\nabla\tilde{\varphi}(x_\alpha^l, t^n))\right]. \tag{2.6}$$

A semi-discrete scheme can be now obtained in the limit $\Delta t \to 0$,

$$\frac{d}{dt}\varphi_\alpha(t) = \lim_{\Delta t \to 0} \frac{\varphi_\alpha^{n+1} - \varphi_\alpha^n}{\Delta t} = \frac{1}{\sum_{l=1}^{m_\alpha} s_l} \sum_{l=1}^{m_\alpha} s_l \left[\hat{d}_l \rho_l \cdot \nabla\tilde{\varphi}_\alpha^l(t) - H(\nabla\tilde{\varphi}_\alpha^l(t))\right], \tag{2.7}$$

where for each l, $\nabla\tilde{\varphi}_\alpha^l(t)$ denotes $\lim_{\Delta t \to 0} \nabla\tilde{\varphi}(x_\alpha^l, t^n)$. All that remains is to determine the coefficients s_l in (2.7). The consistency of the scheme implies that if the value of the gradient is identical in every sector that surrounds x_α, then the numerical Hamiltonian should becomes the differential Hamiltonian. Hence, we are seeking for coefficients s_l, such that

$$\sum_{l=1}^{m_\alpha} s_l \hat{d}_l \rho_l = 0. \tag{2.8}$$

These coefficients can be determined using the results of Abgrall [2]. We denote by $\mu_{l+1/2}$ a unit vector in a direction that is aligned with the interface between the sectors T_l and T_{l+1}, and

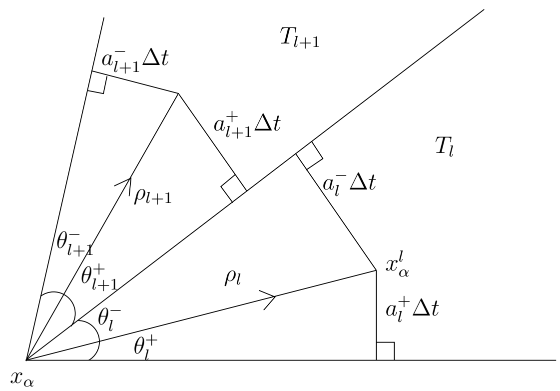

Figure 2.2: The angles around x_α

assume that $\theta_l < \pi$ (which is indeed the case with a triangulation). It was shown in [2] that for any ϵ,

$$\sum_{l=1}^{m_\alpha} \gamma_{l+\frac{1}{2}}\mu_{l+\frac{1}{2}} = 0, \tag{2.9}$$

provided that

$$\gamma_{l+\frac{1}{2}} = \epsilon\left[\tan\left(\frac{\theta_l}{2}\right) + \tan\left(\frac{\theta_{l+1}}{2}\right)\right]. \tag{2.10}$$

In order to incorporate (2.9)–(2.10) into our framework, we split each angle θ_l into two parts $\theta^\pm_l$ that are defined as

$$\theta^\pm_l = \arcsin\frac{a^\pm_l}{\hat{d}_l}, \tag{2.11}$$

(see Fig. 2.2). The consistency condition (2.8) is then satisfied if the weights s_l are taken as $s_l = \beta_l/\hat{d}_l$, where

$$\beta_l = \tan\left(\frac{\theta^+_l + \theta^-_{l-1}}{2}\right) + \tan\left(\frac{\theta^-_l + \theta^+_{l+1}}{2}\right).$$

With these notations, a consistent, semi-discrete scheme is given by

$$\frac{d}{dt}\varphi_\alpha(t) = \frac{1}{\sum_{l=1}^{m_\alpha}\frac{\beta_l}{\hat{d}_l}}\sum_{l=1}^{m_\alpha}\beta_l\left[\rho_l\cdot\nabla\tilde{\varphi}^l_\alpha(t) - \frac{H(\nabla\tilde{\varphi}^l_\alpha(t))}{\hat{d}_l}\right]. \tag{2.12}$$

Remarks.

1. The order of accuracy of the scheme (2.12) is determined by the order of accuracy of the reconstruction $\tilde{\varphi}_\alpha$, and the order of the ODE solver. Due to the known properties of viscosity solutions of HJ equations and the structure of Godunov-type schemes, we

assume a global underlying continuous piecewise-smooth reconstruction. We note that, in practice, the final semi-discrete scheme (2.12) uses only values of the gradient that is computed in the different cells around each grid points x_α. This means that all that we need from the reconstruction is the values of these gradients. High-order reconstructions on triangular meshes are discussed in Section 3.

2. There are several ways to simplify the scheme (2.12). One possibility is to replace the different speeds of propagation at every grid point by their maximum, i.e., $a_\alpha = \max_l\{a_l^+, a_l^-\}$. This implies that $\hat{d}_l = a_\alpha/\sin(\theta_l/2)$. In this case the scheme (2.12) becomes

$$\frac{d}{dt}\varphi_\alpha(t) = \frac{a_\alpha}{\sum_{l=1}^{m_\alpha}\beta_l \sin\frac{\theta_l}{2}} \sum_{l=1}^{m_\alpha}\beta_l\left[\rho_l\cdot\nabla\tilde{\varphi}_\alpha^l(t) - \frac{\sin\frac{\theta_l}{2}}{a}H(\nabla\tilde{\varphi}_\alpha^l(t))\right]. \tag{2.13}$$

If, in addition, the triangulation of the domain is such that the angles are identical around each point, i.e., $\theta=\theta_l$, for all l, then (2.13) takes the simpler form

$$\frac{d}{dt}\varphi_\alpha(t) = \frac{1}{m_\alpha}\sum_{l=1}^{m_\alpha}\left[\frac{a_\alpha}{\sin\frac{\theta}{2}}\rho_l\cdot\nabla\tilde{\varphi}_\alpha^l(t) - H(\nabla\tilde{\varphi}_\alpha^l(t))\right]. \tag{2.14}$$

In the special case of a Cartesian grid with equal spacing in the x- and y-directions, the number of angular sectors at each point is $m_\alpha = 4$, and $\sin(\theta/2) = \sin(\pi/4) = \sqrt{2}/2$. If we assume that the velocities are identical in both directions, the scheme (2.14) becomes

$$\begin{aligned}\frac{d}{dt}\varphi_\alpha(t) = {} & \frac{a_\alpha}{2}\left(\varphi_x^+ - \varphi_x^- + \varphi_y^+ - \varphi_y^-\right) \\ & -\frac{1}{4}\left[H\left(\varphi_x^+,\varphi_y^+\right) + H\left(\varphi_x^-,\varphi_y^+\right) + H\left(\varphi_x^+,\varphi_y^-\right) + H\left(\varphi_x^-,\varphi_y^-\right)\right],\end{aligned} \tag{2.15}$$

with the obvious notations. E.g. $H(\varphi_x^+,\varphi_y^+)$ is the Hamiltonian evaluated at the gradient at x_α that is taken from the first quadrant. The scheme (2.15) is identical to the semi-discrete central scheme for Cartesian grids [9, 20].

3. The following Lax-Friedrichs-type scheme on triangular meshes was derived by Abgrall [2]:

$$\frac{d}{dt}\varphi_\alpha(t) = \frac{a}{\pi}\sum_{l=1}^{m_\alpha}\beta_{l+\frac{1}{2}}\rho_{l+\frac{1}{2}}\cdot\left(\frac{\nabla\tilde{\varphi}_\alpha^l(t) + \nabla\tilde{\varphi}_\alpha^{l+1}(t)}{2}\right) - H\left(\frac{\sum_{l=1}^{m_\alpha}\theta_l\nabla\tilde{\varphi}_\alpha^l}{2\pi}\right). \tag{2.16}$$

Here $\rho_{l+1/2}$ is the unit vector in the direction of the interface between the sectors T_l and T_{l+1}, and $\beta_{l+1/2} = \tan(\theta_l/2) + \tan(\theta_{l+1}/2)$. The derivation of (2.16) involved evolution points that were located on the interfaces between the sectors. This resulted with the form of the dissipative term in (2.16) that contains averages of gradients in adjacent sectors. Also, the scheme (2.16) involves a Hamiltonian that is evaluated at the average of the derivatives that are computed in different sectors (with weights that are proportional to the angles). This term was postulated to be in this form, and could have taken different forms. In our case (2.12), this term takes the form of an average over the Hamiltonian that is evaluated in different sectors and is dictated by the derivation of the scheme.

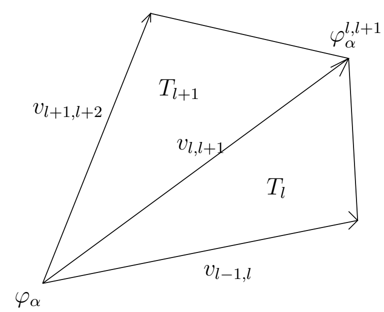

Figure 2.3: grid value at x_α and two triangles containing x_α and grid vectors v

2.2 Monotonicity

In this section we provide a partial result regarding the monotonicity of our scheme (2.12). For simplicity we consider the monotonicity of the scheme in the case where the speeds of propagation do not depend on the gradients of the reconstruction, i.e., they are all equal to a constant that is determined based on a-priori bounds. Hence, we assume $a = \max_{l,\pm} a_l^\pm$, which also implies that $\theta_l^+ = \theta_l^- = \theta_l/2$.

Monotonicity means that if we rewrite our scheme (2.12) in terms of grid differences,

$$\frac{d}{dt}\varphi_\alpha(t) = F(\varphi_\alpha, \varphi_\alpha - \varphi'), \tag{2.17}$$

where $\varphi_\alpha - \varphi'$ is a vector of grid differences that involve the central node, then F is non-increasing in all arguments [27].

We assume that the gradient of φ in the triangle T_l is constant in that triangle. The normal to the plane connecting the three corners of T_l is given by

$$(v_{l,l+1}, \varphi_\alpha^{l,l+1} - \varphi_\alpha) \times (v_{l-1,l}, \varphi_\alpha^{l-1,l} - \varphi_\alpha),$$

and hence the gradient of φ in the sector T_l, $\nabla\varphi_\alpha^l$ is given by (see Fig. 2.3)

$$\frac{1}{C}\left((\varphi_\alpha - \varphi_\alpha^{l-1,l})v_{l,l+1}^y - (\varphi_\alpha - \varphi_\alpha^{l,l+1})v_{l-1,l}^y, (\varphi_\alpha - \varphi_\alpha^{l,l+1})v_{l-1,l}^x - (\varphi_\alpha - \varphi_\alpha^{l-1,l})v_{l,l+1}^x\right).$$

Here, $C = (v_{l,l+1} \times v_{l-1,l}) \cdot k$ and k is the unit vector pointing out of the plane. The superscripts x and y denote the $x-$ and y-components of the various vectors. We note that C is a negative quantity. Letting $u_1 = \varphi_\alpha - \varphi_\alpha^{l,l+1}$, the derivative of the gradient of φ_α^l with respect to u_1 is given by

$$\frac{\partial}{\partial u_1}\nabla\varphi_\alpha^l = \frac{1}{C}(-v_{l-1,l}^y, v_{l-1,l}^x).$$

This means that

$$\rho_l \cdot \frac{\partial}{\partial u_1}\nabla\varphi_\alpha^l = \frac{1}{C}\rho_l \cdot n_{l-1,l}||v_{l-1,l}|| = \frac{1}{C}\sin(\frac{\theta_l}{2})||v_{l-1,l}||,$$

where $n_{l-1,l}$ is the unit normal vector pointing into T_l (and is in the plane defined by T_l). Similarly

$$\frac{\partial}{\partial u_1}\nabla\varphi_\alpha^{l+1} = \frac{1}{C'}(v_{l+1,l+2}^y, -v_{l+1,l+2}^x) = \frac{1}{C'}||v_{l+1,l+2}||n_{l+2,l+1},$$

where $C' = (v_{l+1,l+2} \times v_{l,l+1}) \cdot k$ and $n_{l+2,l+1}$ is the normal vector from T_{l+2} pointing into T_{l+1}.

Since these are the only two quantities in F that involve u_1, we may evaluate the partial derivative of F with respect to u_1. Letting $K = 1/\sum_{l=1}^{m_\alpha} \frac{\beta_l}{\hat{d}_l}$ (which we note is a positive quantity) we have

$$\begin{aligned} \frac{\partial F}{\partial u_1} &= \frac{1}{K}\frac{\beta_l ||v_{l-1,l}||}{C\hat{d}_l}\left(\hat{d}_l \rho_l \cdot n_{l-1,l} - \nabla H(\nabla \varphi_\alpha^l)\cdot n_{l-1,l}\right) \\ &\quad + \frac{1}{K}\frac{\beta_{l+1}||v_{l+1,l+2}||}{C'\hat{d}_{l+1}}\left(\hat{d}_{l+1}\rho_{l+1}\cdot n_{l+2,l+1} - \nabla H(\nabla\varphi_\alpha^{l+1})\cdot n_{l+2,l+1}\right) \\ &= \frac{1}{K}\frac{\beta_l ||v_{l-1,l}||}{C\hat{d}_l}\left(\hat{d}_l \sin(\frac{\theta_l}{2}) - \nabla H(\nabla\varphi_\alpha^l)\cdot n_{l-1,l}\right) \\ &\quad + \frac{1}{K}\frac{\beta_{l+1}||v_{l+1,l+2}||}{C'\hat{d}_{l+1}}\left(\hat{d}_{l+1}\sin(\frac{\theta_{l+1}}{2}) - \nabla H(\nabla\varphi_\alpha^{l+1})\cdot n_{l+2,l+1}\right). \end{aligned} \tag{2.18}$$

We consider only the first term as an analogous argument holds for the second term. Eq. (2.11) implies that $\sin(\theta_l/2) = a/\hat{d}_l$. Also, from (2.1) we know that $\nabla H(\nabla\varphi_\alpha^l)\cdot n_{l-1,l} \le a$, which means that

$$\hat{d}_l \sin(\frac{\theta_l}{2}) - \nabla H(\nabla\varphi_\alpha^l)\cdot n_{l-1,l} \ge 0.$$

Since $C < 0$ and since we assume that the triangulation is such that the β_l's are positive, we can conclude that the first term in (2.18) is non-positive. By similar arguments the second term in (2.18) is non-positive, which means that F is non-increasing in u_1. The same is true for all the variables of F and hence the scheme is monotone.

3 High-Order Reconstructions on Triangular Meshes

In this section we review two third-order reconstructions from [32] (see also [14]). We start with a linear reconstruction. First, we solve an interpolation problem on a large stencil. We then split the large stencil into smaller pieces, obtaining a (low-order) interpolant on each. We conclude with a convex combination of the low-order interpolants that provides the desired (formal) accuracy. The second reconstruction is of WENO-type. Here, we replace the linear weights in the convex combination by non-linear weights. This procedure reduces the spurious oscillations that otherwise develop at singularities. We would like to emphasize that the scheme developed in Section 2, i.e., Eq. (2.12), does not depend on any particular reconstruction and the reconstructions described here are provided for the sake of completeness. Extensions to fourth-order are described in [32].

3.1 A Linear Reconstruction

We overview the linear third-order reconstruction from [32]. The problem can be formulated as an interpolation problem, in which the main question is how to choose the interpolation points. The solution is not so obvious, in particular since the geometry of the mesh might change, which means that stability considerations might imply that it might be better to use different stencils around different triangular sectors.

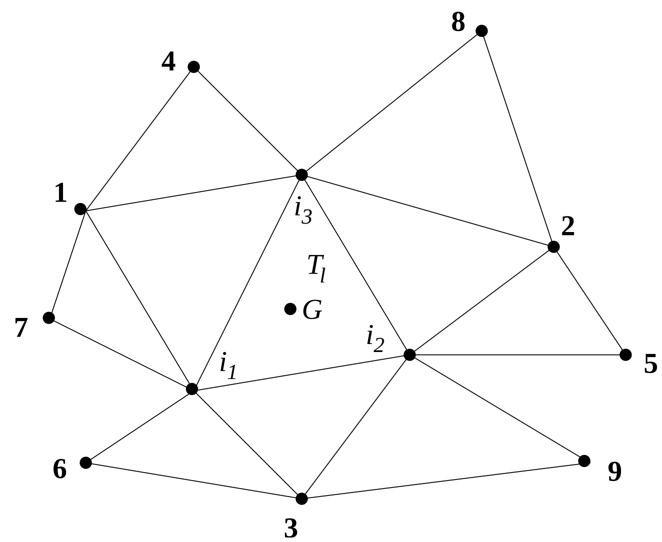

Figure 3.1: The nodes used for the large stencil of the third-order reconstruction around T_l. The point G is the barycenter of the cell T_l

Assuming a given triangular sector, T_l, the procedure for approximating the components of the derivatives at its three nodes is composed of two steps. First, we look for a large stencil that will provide a stable, third-order approximation of the derivative. There are many ways for choosing such a stencil around any given sector, and we are interested in a compact stencil and a stable reconstruction. In the second step we break the large stencil into several small stencils (all of which are based on grid-points that are in the large stencil). Each small stencil provides a second-order approximation of the derivative. These stencils are chosen following compactness and stability considerations. We take sufficiently many such stencils (which will amount to five) such that they can be linearly combined to achieve the desired accuracy of the derivative.

We start by considering an angular sector, T_l, of which its three nodes are denoted by i_1, i_2, i_3. To obtain a third-order approximation of the derivative at these points, $(\nabla\varphi)_{i_1}, (\nabla\varphi)_{i_2}, (\nabla\varphi)_{i_3}$, we first construct a cubic polynomial. Since we are solving a two-dimensional problem, there are ten free parameters that we have to determine. These will be given by interpolation requirements on a stencil that is yet to be determined.

With this in mind, we number the nodes in the neighboring mesh-points as $\{1, \ldots, 9\}$ (in the way that is portrayed in Fig. 3.1), and consider the ordered set $W = \{1, \ldots, 9\}$. The nodes are numbered as in Fig. 3.1 in order to avoid biasing the stencil in a particular direction. We note that the geometry of the mesh might imply that some of these points can be identical. If this is the case, more remote points are added to the list. We omit the details and refer to [32]. We now set a threshold δ and use the following algorithm:

1. Set the interpolation points as $S_0 = \{i_1, i_2, i_3, 1, \ldots 7\}$.

2. Form the 10×10 interpolation coefficients matrix A and compute its reciprocal condition number, $c(A)$.

3. While $c(A) < \delta$, add the next node in W to S_0 and compute the least squares interpolation coefficients matrix A from the nodes in S_0. Compute $c(A)$.

4. The final S_0 is the large stencil.

Remark. The numerical simulations of [32] showed that at most 12 nodes are needed in order to satisfy the condition $c(A) \geq \delta$ when the threshold is set as $\delta = 10^{-3}$. This is the value that was used in our simulations in Section 4.

We denote the interpolation polynomial that is obtained from the stencil S_0 by $p^3(x, y)$. This polynomial, $p^3(x, y)$, can be used to estimate a third-order approximation of the derivatives at the three nodes of T_l. Our goal now is to split the stencil S_0 into several small stencils in such a way that we will be able to recover the third-order accuracy with a convex combination of these smaller stencils. In this case, we will generate five quadratic polynomials, p_s, $s = 1, \ldots, 5$, such that a third-order approximation to the derivatives in the x- and y-direction at $\{i_1, i_2, i_3\}$, will be given by

$$\frac{\partial}{\partial x}\varphi(x_{i_j}, y_{i_j}) \approx \frac{\partial}{\partial x}p^3(x_{i_j}, y_{i_j}) = \sum_{s=1}^{5} \gamma_{s,x,i_j} \frac{\partial}{\partial x} p_s(x_{i_j}, y_{i_j}), \qquad j = 1, 2, 3, \tag{3.1}$$
$$\frac{\partial}{\partial y}\varphi(x_{i_j}, y_{i_j}) \approx \frac{\partial}{\partial y}p^3(x_{i_j}, y_{i_j}) = \sum_{s=1}^{5} \gamma_{s,y,i_j} \frac{\partial}{\partial y} p_s(x_{i_j}, y_{i_j}), \qquad j = 1, 2, 3.$$

Here, γ_{s,x,i_j} and γ_{s,y,i_j} are the linear weights for the derivatives in the x- and y-directions, respectively. They depend only on the local geometry of the mesh and should satisfy the normalization constraints, $\sum_{s=1}^{5} \gamma_{s,x,i_j} = 1$ and $\sum_{s=1}^{5} \gamma_{s,y,i_j} = 1$. Under these additional conditions, a simple calculation shows that the number of quadratic interpolants has to be greater than or equal to five, which is the reason as of why we set it as five [14, 32].

We are now seeking for five small stencils Γ_s, $s = 1, \ldots, 5$, for the target triangle T_l such that $S_0 = \cup_{s=1}^{5} \Gamma_s$. We associate with each such stencil a quadratic polynomial p_s. We note that while the stencils are going to be identical for all the nodes in a given angular sector and in both directions, the linear weights γ_{s,x,i_j} and γ_{s,y,i_j} can be different for each node and for each direction. We summarize the stages given in [32, Procedure 2.2] as follows (for further details see [32]):

1. Obtain a large stencil S_0.

2. For each $s = 1, \ldots, 5$ find a set of candidate small stencils $W_s = \{\Gamma_s^{(r)}, r = 1, \ldots, n_s\}$ in the following way. The nodes i_1, i_2, i_3 are included in every $\Gamma_s^{(r)}$. Let $A_s^{(r)}$ denote the center of $\Gamma_s^{(r)}$, where $A_s^{(r)}$ is given in Table 3.1. Find at least 3 additional nodes other than i_1, i_2, i_3 such that they have the shortest distance from $A_s^{(r)}$ and the points in $\Gamma_s^{(r)}$ induce an interpolation coefficient matrix A with a good reciprocal condition number ($c(A) \geq \delta$). Based on the experiments in [32] a maximum number of 8 nodes are required to reach the threshold $\delta = 10^{-3}$.

3. Obtain $n_1 \times \cdots \times n_5$ groups of small stencils by taking one small stencil $\Gamma_s^{(r_s)}$ from each W_s, $s = 1, \ldots, 5$. Eliminate the groups that contain the same small stencils and those that do not satisfy the condition $\cup_{s=1}^{5} \Gamma_s^{(r_s)} = S_0$.

4. For each group $\{\Gamma_s^{(r_s)}, s = 1, \ldots, 5\}$ compute the associated linear weights $\gamma_{s,x,i_j}^{(r_s)}$ and $\gamma_{s,y,i_j}^{(r_s)}$, such that (3.1) is satisfied for $\{i_1, i_2, i_3\}$. Candidate stencils that involve solving ill-posed linear systems are eliminated from further considerations.

5. For the remaining groups, find the minimum value γ_l of all the linear weights $\gamma^{(r_s)}_{s,x,i_j}, \gamma^{(r_s)}_{s,y,i_j}$ on the three vertices $\{i_1, i_2, i_3\}$. The group for which γ_l is the biggest is taken as the final five small stencils for the sector T_l. These five small stencils are denoted by Γ_s, $s = 1, \dots, 5$.

s	n_s	$A_s^{(1)}$	$A_s^{(2)}$	$A_s^{(3)}$
1	1	G	–	–
2	3	1	4	7
3	3	2	5	8
4	3	3	6	9
5	≤ 9	$A_5^{(r)}$ are 4-9 and the middle points of 4–8, 5–9, 6–7		

Table 3.1: The values of $A_s^{(r)}$. The entries refer to the node numbers in Fig. 3.1

Remark. Since the linear weights depend on the geometry of the triangulation, some of them might be negative. It is therefore required to take special measures to avoid the stability problems that result from negative weights in the presence of large gradients. In the numerical simulations we apply the technique for handling negative weights in WENO schemes that was recently proposed in [30].

3.2 A WENO Reconstruction

In the previous section we showed how to obtain a third-order reconstruction of the derivatives in the x- and y-direction in each grid point. This was done by finding an accurate linear combination of small stencils (each of which results with a second-order reconstruction) such that the overall combination is a third-order reconstruction of the derivative. We now use these results to derive a WENO reconstruction of the derivative. This is done, as usual, by replacing the linear weights by nonlinear weights aiming at reducing the spurious oscillations that might develop in regions that contain discontinuities.

We consider the x-directional derivative at the vertex i of the cell T_l, whose coordinates are (x_i, y_i). Following Section 3.1, we denote by $p_s(x, y)$, $s = 1, \dots, 5$, the sth interpolation polynomial associated with the sth stencil on the cell T_l. A third-order WENO reconstruction for the x-derivative is given in terms of the convex combination

$$(\varphi_x)_i = \sum_{s=1}^{5} w_s \frac{\partial}{\partial x} p_s(x_i, y_i). \tag{3.2}$$

The weights, w_s, associated with $p_s(x, y)$ are given by

$$w_s = \frac{\tilde{w}_s}{\sum_{m=1}^{5} \tilde{w}_m}, \tag{3.3}$$

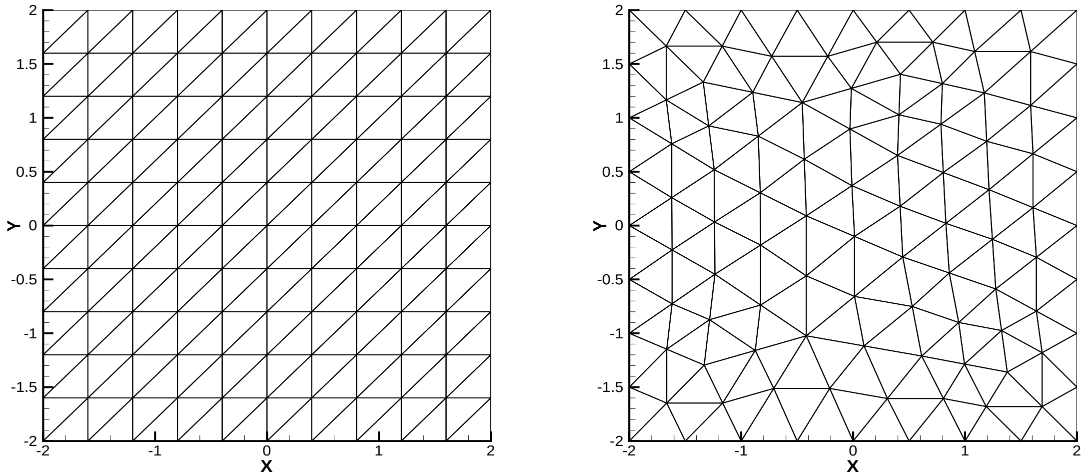

Figure 4.1: *Left:* coarsest uniform mesh with $h = 2/5$; *Right:* coarsest non-uniform mesh with $N = 105$ nodes.

with

$$\tilde{w}_s = \frac{\gamma_{s,x}}{(\epsilon + \beta_s)^2}, \qquad s = 1, \dots, 5. \tag{3.4}$$

Here, $\gamma_{s,x}$ is the linear weight associated with stencil s for computing the x-derivative at (x_i, y_i), ϵ is set as a small number to prevent the denominator from vanishing, and β_s is the oscillation indicator associated with the sth stencil.

The oscillatory indicator, β_s, is given by

$$\beta_s = \sum_{|\eta|=2} \int_{T_l} (D^\eta p_s(x,y))^2 dxdy. \tag{3.5}$$

An expression analogous to (3.2) holds for the derivative in the y-direction.

4 Numerical Examples

In most of the numerical examples we use two kinds of triangular meshes. Both are shown in Fig. 4.1. The first kind is a "uniform triangular mesh" shown in Fig. 4.1 (left). The particular mesh in Fig. 4.1 (left) is a coarse mesh with $h = 2/5$ where h is the length of the right-angled side. The second mesh is a "nonuniform triangular mesh" such as the one shown in Fig. 4.1 (right). The mesh in the figure is a coarse mesh with $N = 105$ nodes. Refinements of non-uniform meshes are done by splitting each triangle into four similar triangles. The reconstructions we use in all the simulations are the third-order linear and WENO reconstructions from Section 3. We refer to the flux (2.12) together with the linear reconstruction of Section 3.1 as the "linear scheme". We refer to (2.12) together with the WENO reconstruction of Section 3.2 as the "WENO scheme". The ODE solver we used is the third-order strong stability preserving Runge-Kutta (SSP-RK) method [12].

	Linear scheme				WENO scheme			
N	L^1-error	order	L^∞-error	order	L^1-error	order	L^∞-error	order
105	2.03E-01	—	3.50E-01	—	4.63E-01	—	7.24E-01	—
385	3.16E-02	2.68	6.12E-02	2.51	1.69E-01	1.46	2.62E-01	1.47
1473	4.17E-03	2.92	9.02E-03	2.76	3.32E-02	2.34	7.10E-02	1.88
5761	5.30E-04	2.97	1.20E-03	2.91	5.09E-03	2.70	1.70E-02	2.07
22785	6.68E-05	2.99	1.54E-04	2.96	5.84E-04	3.12	2.53E-03	2.74

Table 4.1: Accuracy test for the 2D Linear equation (4.1) on non-uniform meshes with the third-order Linear and WENO Schemes at $t = 2$.

Example 1. A 2D Linear Equation

Consider the two-dimensional linear equation

$$\begin{cases} \phi_t + \phi_x + \phi_y = 0, & -2 \le x < 2, -2 \le y < 2, \\ \phi(x, y, 0) = \sin(\frac{\pi}{2}(x+y)), & \end{cases} \tag{4.1}$$

with periodic boundary conditions.

We solve (4.1) with the linear and the WENO scheme on non-uniform meshes up to time $t = 2$. Since this is a linear problem with constant coefficients, the flux with the local speeds and the flux with the global speeds are identical. The L^1- and L^∞-errors and orders of accuracy, that are shown in Table 4.1, confirm the expected third-order accuracy.

Example 2. A 2D Burgers Equation

Consider the two-dimensional Burgers equation

$$\begin{cases} \phi_t + \dfrac{1}{2}(\phi_x + \phi_y + 1)^2 = 0, & -2 \le x < 2, -2 \le y < 2, \\ \phi(x, y, 0) = -\cos\left(\frac{\pi}{2}(x+y)\right), & \end{cases} \tag{4.2}$$

augmented with periodic boundary conditions.

We use this example to investigate the difference between flux that use a global constant speed and those that use local speeds. A scheme with a global constant speed is obtained from (2.13) when we replace a_α by $a = \max_\alpha a_\alpha$. We solve (4.2) on non-uniform meshes up to time $t = 0.5/\pi^2$. This is before the solution develops any singularities. Table 4.2 shows the L^1- and L^∞-accuracy results that are obtained with the scheme that used a global constant speed. Table 4.3 shows the L^1- and L^∞-errors and orders of accuracy that are obtained when local speeds are taken into account in the numerical flux. In both cases we use linear and WENO schemes. In all cases we verify the expected third-order of accuracy. Indeed, the errors obtained when using a global speed are larger than the error obtained when accounting for local speeds.

In Fig. 4.2 we plot the solution of (4.2) at time $t = 1.5/\pi^2$, after the solution developed discontinuous derivatives. The solution is obtained with a third-order WENO scheme and a uniform mesh with mesh spacing $h = 1/10$.

	Linear scheme				WENO scheme			
N	L^1-error	order	L^∞-error	order	L^1-error	order	L^∞-error	order
105	2.28E-02	—	6.89E-02	—	6.53E-02	—	1.63E-01	—
385	3.80E-03	2.58	1.81E-02	1.93	1.64E-02	2.00	5.94E-02	1.46
1473	5.32E-04	2.83	3.90E-03	2.22	3.50E-03	2.23	1.66E-02	1.84
5761	6.99E-05	2.93	6.99E-04	2.48	5.98E-04	2.55	3.63E-03	2.19
22785	8.96E-06	2.96	8.87E-05	2.98	7.26E-05	3.04	4.95E-04	2.87

Table 4.2: Accuracy for the 2D Burgers equation (4.2) on non-uniform meshes with third-order Linear and WENO Schemes at $t = 0.5/\pi^2$. A Global constant speed.

	Linear scheme				WENO scheme			
N	L^1-error	order	L^∞-error	order	L^1-error	order	L^∞-error	order
105	1.30E-02	—	2.98E-02	—	3.94E-02	—	1.01E-01	—
385	1.87E-03	2.79	6.03E-03	2.31	9.86E-03	2.00	4.95E-02	1.04
1473	2.49E-04	2.91	1.56E-03	1.95	2.24E-03	2.14	1.48E-02	1.74
5761	3.20E-05	2.96	2.23E-04	2.81	3.97E-04	2.50	3.49E-03	2.09
22785	4.05E-06	2.98	3.21E-05	2.80	4.70E-05	3.08	4.88E-04	2.84

Table 4.3: Accuracy for the 2D Burgers equation (4.2) on non-uniform meshes with third-order Linear and WENO Schemes at $t = 0.5/\pi^2$. Local speeds of propagation.

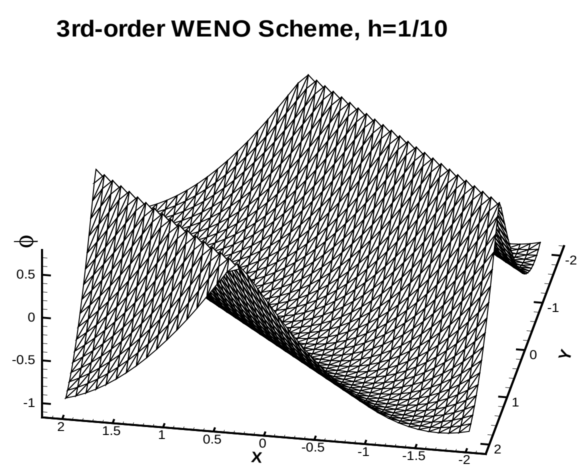

Figure 4.2: The 2D Burgers equation (4.2) at $t = 1.5/\pi^2$ on a uniform mesh with $h = 1/10$. The solution is obtained with a third-order WENO scheme and a local speeds flux.

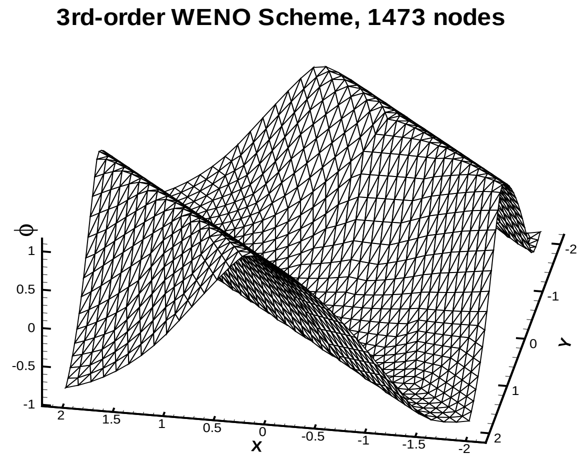

Figure 4.3: A 2D HJ equation with a non-convex flux (4.3) at $t = 1.5/\pi^2$. The solution is obtained with a third-order WENO scheme on a nonuniform mesh with $N = 1473$ nodes and a local speed flux.

Example 3. A Non-Convex Flux

Consider the following HJ equation with a non-convex flux:

$$\begin{cases} \phi_t - \cos(\phi_x + \phi_y + 1) = 0, & -2 \le x < 2, -2 \le y < 2, \\ \phi(x,y,0) = -\cos(\frac{\pi(x+y)}{2}), \end{cases} \tag{4.3}$$

augmented with periodic boundary conditions.

In this example we use a non-uniform mesh with $N = 1473$ nodes. At $t = 1.5/\pi^2$ the solution develops a discontinuous derivative. In Fig. 4.3 we show the results obtained using the third-order WENO scheme with the local speed flux.

Example 4. A 2D Riemann Problem

Consider the following two-dimensional Riemann problem:

$$\begin{cases} \phi_t + \sin(\phi_x + \phi_y) = 0, & -1 < x < 1, -1 < y < 1, \\ \phi(x,y,0) = \pi(|y| - |x|). \end{cases} \tag{4.4}$$

We solve (4.4) on a uniform triangular mesh with $40 \times 40 \times 2$ elements. The scheme we use is a third-order WENO scheme with a local speeds flux. Fig. 4.4 shows the results obtained at time $t = 1$.

Example 5. An Optimal Control Problem

Consider the following optimal control problem

$$\begin{cases} \phi_t + (\sin y)\phi_x + (\sin x + \mathrm{sgn}(\phi_y))\phi_y - \frac{1}{2}\sin^2 y - (1 - \cos x) = 0, & -\pi < x < \pi, -\pi < y < \pi, \\ \phi(x,y,0) = 0, \end{cases}$$

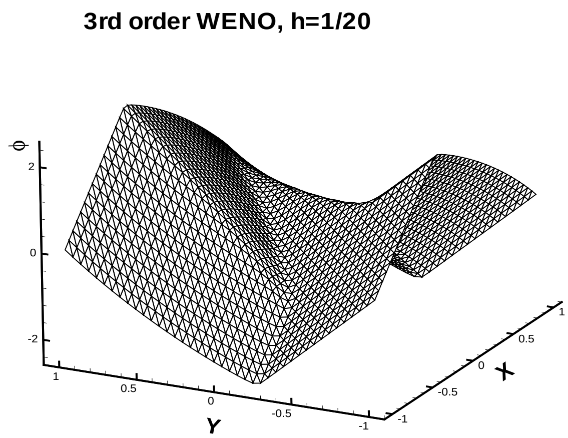

Figure 4.4: The 2D Riemann problem (4.4) at $t = 1$. The solution is obtained with a third-order WENO scheme and a local speeds flux on a uniform triangular mesh with $h = 1/20$.

(4.5)

with periodic boundary conditions, see [29].

We approximate solutions of (4.5) on a the uniform triangular mesh with $40 \times 40 \times 2$ elements using a third-order WENO scheme with local speed flux. The solution at $t = 1$ is shown in Fig. 4.5 (left). The corresponding optimal control $\omega = \text{sgn}(\phi_y)$ is shown in Fig. 4.5 (right).

Example 6. A 2D Eikonal equation

Consider the following two-dimensional Eikonal equation which arises in geometric optics [17]:

$$\begin{cases} \phi_t + \sqrt{\phi_x^2 + \phi_y^2 + 1} = 0, & 0 \le x < 1, 0 \le y < 1, \\ \phi(x, y, 0) = 0.25(\cos(2\pi x) - 1)(\cos(2\pi y) - 1) - 1. \end{cases} \tag{4.6}$$

We approximate solutions of (4.6) using the third-order WENO scheme with the local speeds flux. We use the non-uniform mesh that is shown in Fig. 4.6 (left). The solution at $t = 0.6$ is shown in Fig. 4.6 (right).

5 Conclusion

In this paper we derived the first central scheme for Hamilton-Jacobi equations on unstructured grids. Similarly to any other Godunov-type method, this scheme is obtained by an exact evolution of a reconstruction which is then projected back onto the mesh points. The order of accuracy of the scheme is determined by the accuracy of the reconstruction and the accuracy of the ODE solver. The reconstructions we chose to work with are the third-order linear and WENO reconstructions on triangular meshes [32].

While we have proved the monotonicity of the scheme in the special case of a global constant local speeds of propagation, we believe that the scheme is monotone in the general case (for a

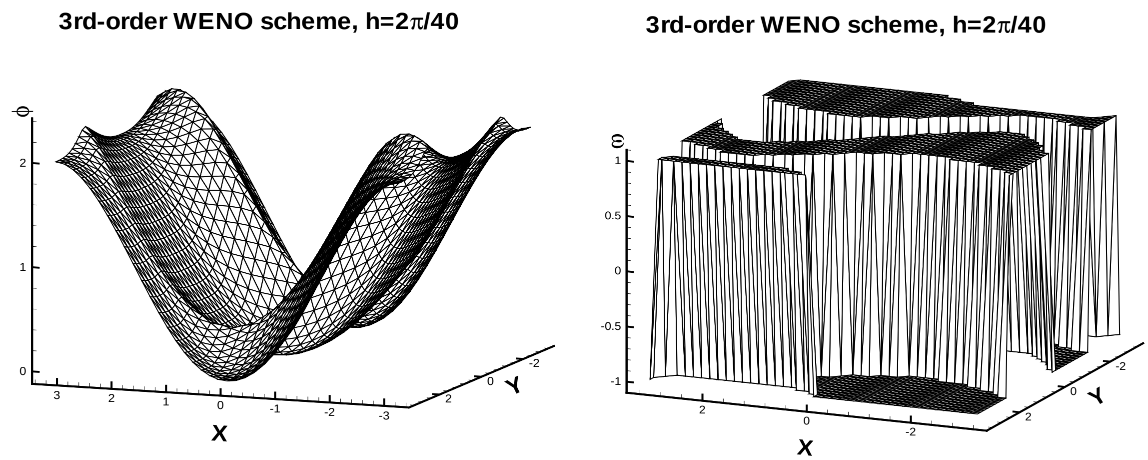

Figure 4.5: An optimal control problem (4.5) at $t = 1$ solved on a uniform triangular mesh with $h = 2\pi/40$. The solution is obtained with a third-order WENO scheme and a local speeds flux. *Left:* the solution; *Right:* the optimal control $\omega = \text{sgn}(\phi_y)$.

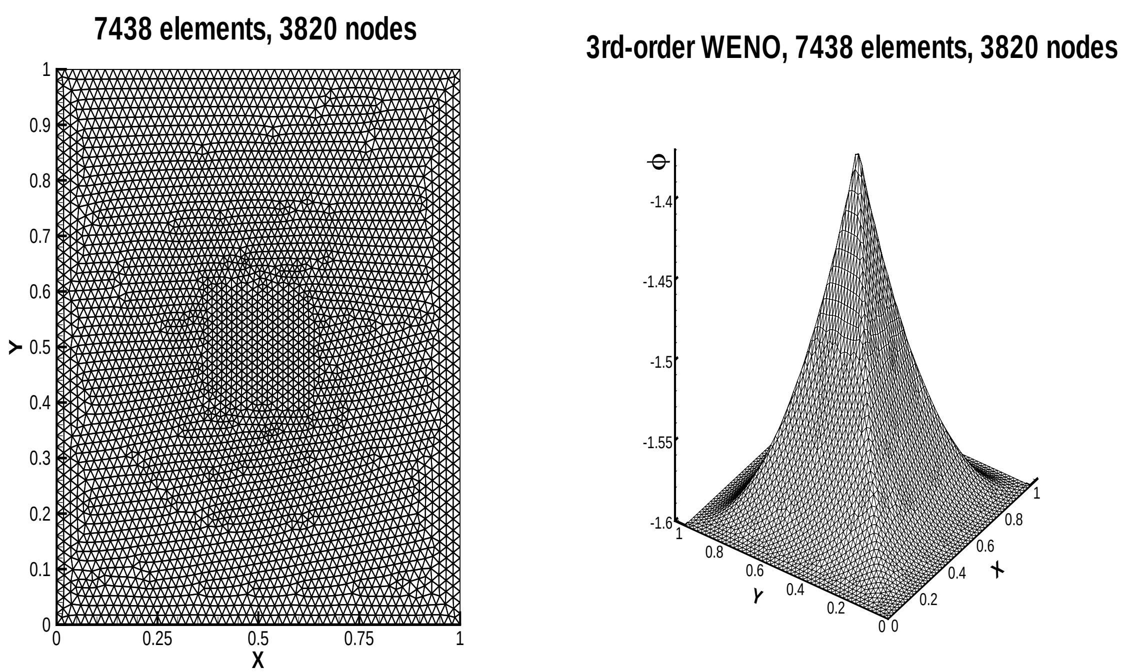

Figure 4.6: The 2D Eikonal equation (4.6). *Left:* the non-uniform mesh used in this example; *Right:* the solution at $t = 0.6$ obtained with the third-order WENO scheme with local speeds flux.

proper choice of the speeds where some global bounds are taken into consideration [29]). This point remains as an open problem which we hope to address in the future.

References

[1] R. Abgrall, *On essentially non-oscillatory schemes on unstructured meshes: Analysis and implementation*, J. Comput. Phys., **114** (1994), pp.45–54.

[2] R. Abgrall, *Numerical discretization of the first-order Hamilton-Jacobi equation on triangular meshes*, Commun. Pure Appl. Math., **49** (1996), pp.1339–1373.

[3] S. Augoula and R. Abgrall, *High order numerical discretization for Hamilton-Jacobi equations on triangular meshes*, J. Sci. Comput., **15** (2000), pp.197–229.

[4] G. Barles and P.E. Souganidis, *Convergence of approximation schemes for fully nonlinear second order equations*, Asym. Anal., **4** (1991), pp.271–283.

[5] T. Barth and J. Sethian, *Numerical schemes for the Hamilton-Jacobi and level set equations on triangulated domains*, J. Comput. Phys., **145** (1998), pp.1–40.

[6] S. Bryson, A. Kurganov, D. Levy and G. Petrova, *Semi-discrete central-upwind schemes with reduced dissipation for Hamilton-Jacobi equations*, IMA J. Numer. Anal. to appear.

[7] S. Bryson and D. Levy, *Central schemes for multidimensional Hamilton-Jacobi equations*, SIAM J. Sci. Comput., **25** (2003), pp.767–791.

[8] S. Bryson and D. Levy, *High-order central WENO schemes for multi-dimensional Hamilton-Jacobi equations*, SIAM J. Numer. Anal., **41** (2003), pp.1339–1369.

[9] S. Bryson and D. Levy, *High-order semi-discrete central-upwind schemes for multi-dimensional Hamilton-Jacobi equations*, J. Comput. Phys., **189** (2003), pp.63–87.

[10] M.G. Crandall, H. Ishii and P.-L. Lions, *User's guide to viscosity solutions of second order partial differential equations*, Bull. Amer. Math. Soc., **27** (1992), pp.1–67.

[11] M.G. Crandall and P.-L. Lions, *Two approximations of solutions of Hamilton-Jacobi equations*, Math. Comp., **43** (1984), pp.1–19.

[12] S. Gottlieb, C.-W. Shu and E. Tadmor, *Strong stability-preserving high order time discretization methods*, SIAM Rev., **43** (2001), pp.89–112.

[13] A. Harten, B. Engquist, S. Osher and S. Chakravarthy, *Uniformly High Order Accurate Essentially Non-oscillatory Schemes III*, J. Comput. Phys., **71** (1987), pp.231–303.

[14] C. Hu and C.-W. Shu, *Weighted essentially non-oscillatory schemes on triangular meshes*, J. Compt. Phys., **150** (1999), pp.97–127.

[15] G.-S. Jiang and D. Peng, *Weighted ENO schemes for Hamilton-Jacobi equations*, SIAM J. Sci. Comput., **21** (2000), pp.2126–2143.

[16] G.-S. Jiang and C.-W. Shu, *Efficient implementation of weighted ENO schemes*, J. Comput. Phys., **126** (1996), pp.202–228.

[17] S. Jin and Z. Xin, *Numerical passage from systems of conservation laws to Hamilton-Jacobi equations, and relaxation schemes*, SIAM J. Numer. Anal., **35** (1998), pp.2385–2404.

[18] G. Kossioris, Ch. Makridakis and P.E. Souganidis, *Finite volume schemes for Hamilton-Jacobi equations*, Numer. Math., **83** (1999), pp.427–442.

[19] A. Kurganov, S. Noelle and G. Petrova, *Semidiscrete central-upwind schemes for hyperbolic conservation laws and Hamilton-Jacobi equations*, SIAM J. Sci. Comput., **23** (2001), pp.707–740.

[20] A. Kurganov and E. Tadmor, *New high-resolution semi-discrete schemes for Hamilton-Jacobi equations*, J. Comput. Phys., **160** (2000), pp.241–282.

[21] D. Levy and S. Nayak, *Central schemes for Hamilton-Jacobi on unstructured grids*, Proc. ENUMATH 2003, to appear.

[22] C.-T. Lin and E. Tadmor, *L^1-stability and error estimates for approximate Hamilton-Jacobi solutions*, Numer. Math., **87** (2001), pp.701–735.

[23] C.-T. Lin and E. Tadmor, *High-resolution non-oscillatory central schemes for Hamilton-Jacobi Equations*, SIAM J. Sci. Comput., **21** (2000), pp.2163–2186.

[24] P.L. Lions, *Generalized solutions of Hamilton-Jacobi equations*, Pitman, London, 1982.

[25] P.L. Lions and P.E. Souganidis, *Convergence of MUSCL and filtered schemes for scalar conservation laws and Hamilton-Jacobi equations*, Numer. Math., **69** (1995), pp.441–470.

[26] X.-D. Liu, S. Osher and T. Chan, *Weighted essentially non-oscillatory schemes*, J. Comput. Phys., **115** (1994), pp.200–212.

[27] A. Oberman, *Convergent difference schemes for degenerate elliptic and parabolic equations: Hamilton-Jacobi equations and free boundary problems*, submitted.

[28] S. Osher and J. Sethian, *Fronts propagating with curvature dependent speed: algorithms based on Hamilton-Jacobi formulations*, J. Comp. Phys., **79** (1988), pp.12–49.

[29] S. Osher and C.-W. Shu, *High-order essentially nonoscillatory schemes for Hamilton-Jacobi equations*, SIAM J. Numer. Anal., **28** (1991), pp.907–922.

[30] J. Shi, C. Hu and C.-W. Shu, *A technique of treating negative weights in WENO schemes*, J. Comp. Phys., **175** (2002), pp.108–127.

[31] P.E. Souganidis, *Approximation schemes for viscosity solutions of Hamilton-Jacobi equations*, J. Differential Equations, **59** (1985), pp.1–43.

[32] Y.-T. Zhang and C.-W. Shu, *High-order WENO schemes for Hamilton-Jacobi equations on triangular meshes*, SIAM J. Sci. Comput., **24** (2003), pp.1005–1030.